IEEE Transactions on Nuclear Science, Vol. NS-28, No. 3, June 1981

F-

BEAM OPTICAL PROPERTIES OF THE NSLS DIPOLES*

J. N. Galayda, L. N. Blumberg, R. N. Heese, H.C.H. Hsieh
National Synchrotron Light Source
Brookhaven National Laboratory
Upton, N.Y. 11973

Abstract

Presently there is much interest in low energy (< 1 GeV) electron storage rings as sources of synchrotron radiation and for studies of the free electron laser. The economics and physics of these storage rings favor the use of bending magnets with small radius of curvature and large bend angle. Here we discuss some general features of such magnets and the results of magnetic mesurements of the dipole magnets of the NSLS booster and storage rings. We interpret the magnetic measurements in terms of the magnet geometry and saturation characteristics. We discuss transport functions describing the linear and nonlinear focusing properties of the magnets, parametrized in terms of their curvature and fringe field length.

DATA ANALYSIS

Measurements of the vertical field components in the median plane were obtained for all magnets at 5 mm intervals (2.5 mm near the magnet ends) along arcs of five circles with equal radius and centers displaced by 1 cm. The average field along these arcs, $\int B_z d\ell/L$ was fitted to a quadratic function to obtain the mean dipole, quadrupole and sextupole terms summarized in Table I. These values were used for comparison of magnets of the same type; the quoted quadrupole and sextupole terms measure the variation of the integrated field relative to the transverse y coordinate (Fig. 1). The dipole term is seen to vary by less than ± 0.1% for the booster and VUV magnets and ± 0.15% for the X=ray magnets.

The data were also fitted to a multipole expansion around the ideal beam path using a linear least-squares algorithm. The expansion consisted of the two-dimensional harmonics with coefficients which are linear functions of position along the beam path. The beam path was divided into segments and a set of coefficients was computed for each segment. This allowed investigation of the variation of multipole harmonics along the beam path caused by the geometry of the magnets.

MAGNET PROPERTIES

The construction of the NSLS dipole magnets has been described previously.[1] The optical properties of the 700 MeV ring and booster dipoles are strongly influenced by the construction features of these magnets. A single lamination design, and thus one stamping die, was used for the magnets of all rings. Only a modification in the pole tip region of the die was required to make the laminations of the combined-function booster dipoles. The bending magnets of all rings are curved to follow the path of the beam. However, these magnets do not have an axis of rotational symmetry; they are assembled so that the inner and outer edges of the pole follow circles of equal radius whose centers are separated by one pole width. This is to be contrasted with a sector magnet, in which the inner and outer edges of the pole describe concentric circles whose radii differ by the width of the pole. Figure 1 shows a booster or VUV dipole viewed from above. The magnet is made up of eight blocks, each of which is parallelogram-shaped. All laminations in the magnets are parallel, but staggered to follow the beam path, a 45° arc of radius 1.91 meters. Thus there are no wedge-shaped gaps or fillers in the magnet core. As a result of this assembly technique, the angle θ between the orbit radius vector and the laminations varies from 0° at the center of the magnet to almost 22.5° at the ends. These features have several effects on the optical properties of the magnets: 1) Fringe field focusing is quite significant in these magnets, compared to the ring quadrupoles; 2) The width of the poletip, measured perpendicular to the beam path, is equal to the poletip width of the lamination multiplied by cosθ. The slope of the poleface and thus the field gradient should increase by a factor 1/cosθ along the beam path. Since the sextupole field depends on the square of displacement, this harmonic might be expected to vary as $1/\cos^2\theta$ along the beam path.

The magnet design program POISSON[2] was used to design the dipole magnet laminations, as well as to model the booster and storage ring dipoles with all horizontal dimensions scaled down by cosθ, $0 \leq \theta \leq 22.5°$. This attempt[3] to assess the three dimensional properties of a magnet with two dimensional calculations assumes that the poletip width variation is sufficiently gradual and that the tensor character of the permeability of a stack of laminations can be ignored.

First we consider the gradient in the booster dipole. Computed results confirmed the conjecture that the gradient G(θ) on the beam path at a point where the radius vector makes an angle θ with the laminations is greater than the gradient in the center of the magnet G(0) by a factor secθ. The result wasfound both for infinite and finite permeability at 12.23 kG central field. Figure 2 is a plot of G(θ)/G(0) versus secθ in the booster dipole, at central fields of 8 Kg and 12 KG. Each point shows the average of the fitted gradients in three of the magnets. The vertical line marks the end of the magnet core. The rms deviation around the average is typically ± 0.004. We see that agreement with the solid line predicted by POISSON is reasonable out to secθ = 1.05. The divergence of the 8 KG and 12 KG data may be due to saturation of the magnet ends, which causes a 2% drop in B_z at secθ = 1.06 in the high field case.

Figure 3 shows POISSON predictions and field measurements at 8 KG and 12 KG for the normalized sextupole term B''(θ)/B''(0) plotted versus $\sec^2\theta$ in the booster dipole. Both the POISSON predictions and the measurements show a faster increase than $\sec^2\theta$. Again each data point is the average of the fitted sextupole terms from three magnets. The typical rms deviation around the average is ± 0.03. The 12 KG data deviates grossly from POISSON prediction, probably due to saturation of the magnet ends.

POISSON predictions for the dipole component along the beam path showed a practically constant field for $0<\theta<22.5°$ and $0<B<12.2$ KG. Figure 4 shows the measured dipole components along the beam path in the X-ray and VUV bending magnets excited to an average field of 8 KG. The vertical line marks the end of the magnet cores. There is no evidence of

*Research supported by the U.S. Department of Energy.

0018-9499/81/0600-2593$00.75©1981 IEEE

dependence of the dipole component on at this field. Figure 5 shows the same information with magnets excited to 12.2 KG. The VUV magnet data shows a smooth decrease in dipole field beginning at the center of the magnet (x = 0 mm) so one might suspect some dependence of the dipole components. The X-ray dipole is designed to bend the beam through a 22.5° arc of radius 6.88 meters, so we may test the possibility of θ-dependent iron saturation. The data in Figure 5 is arranged so the X-ray magnet end coincides with the VUV magnet end. The data from the two magnets overlap more convincingly than in Figure 6, which shows the dipole components for the same magnets plotted against . Thus it is likely that the sag in the dipole field is caused by saturation of the magnet end which extends far into the body of the magnet, rather than by saturation related to the stacking geometry. The effective length[4] of these magnets, defined as

$$L_{eff} = \frac{\int B_z(\theta) R d\theta}{B_z(\theta=0)}$$

shrinks by 12 mm in going from 8 KG to 12.2 KG. Figure 7 shows the calculated deviation from the ideal orbit of (R = 1909.9 mm) particle bent 45° by the prototype VUV dipole magnet, excited to 12.2 KG. After leaving the magnetic field, the deviation is negligible.

At 12.2 KG excitation, iron saturation causes the field at = 0 to be 3.7% less than for infinite permeability. Sag in the dipole component begin to be measureable for B = 10 KG at θ = 0. Even though only 0.5% more current is necessary at this field than for infinite permeability, the effective length of the magnet has decreased by 4 mm.

A second method for analysing the median plane field maps was ray-tracing to obtain elements of the matrix describing beam transport through the magnet. The median plane trajectory was obtained by numerical integration of the equation of motion.

$$y'' + \frac{1}{\rho}\left(1 + (y')^2\right)^{3/2} = 0 \qquad (1)$$

Variation of the rigidity $B\rho$ to obtain the desired 45° bend resulted in the trajectory of Fig. 7 for a VUV dipole, where the relative displacement y_R is given with respect to the orbit of a particle through an ideal magnet with bending radius 1909.9 mm. It is seen that the trajectory does not deviate more than 1.25 mm from the reference arc. After leaving the magnetic field, the deviation is only 0.2 mm. Integration of the field along the trajectory of Fig. 7 yields the effective length, Leff = 1496.4 mm, is in excellent agreement with the 1500 mm value used in the lattice design calculations. For the vertical trajectory we solve the equation of motion

$$mv \frac{d^2z}{ds^2} = e\left[B_x \sin\theta - B_y \cos\theta\right] \qquad (2)$$

where is the angle between v and B_x and the unmeasured components are obtained from the $\nabla \times B = 0$ relationship as

$$B_x \approx \left(\partial B_z/dx\big|_o\right) z \text{ and } B_y \approx \left(\partial B_z/dy\big|_o\right) z.$$

We obtain matrix elements by computing the trajectories of particles displaced initially from the central ray by distance or angle ' and giving final displacements Y or Y' as $M_{11} = Y_r/$, $M_{21} = Y'_r/$, $M_{12} = Y_r/\varepsilon'_r$, $M_{22} = Y'_r/\varepsilon'_r$. In Fig. 8 we show the variation of the M_{21} elements with for both the VUV prototype and VUV magnet 1. A 1 mm thick shim on the end plate of the latter was used to reduce the quadrupole and sextupole contribution from the fringe field. The sextupole strength $S = B''L/B\rho$ can be shown to be related to M_{21} by $S = 2\,(dm_{21}/d\varepsilon_r)$ with = cos (22.5°). The sextupole strength in VUV magnet No. 1 was thus reduced by a factor of 3 as a result of shimming. Comparisons of the small amplitude matrix elements with theoretical expressions were made where applicable. The value M_{21} = -0.0473 radian/meter in VUV dipole 1 compares favorably with the value M_{21} = - .0467 which would be deduced from the integrated gradients shown in Table I. The optical effects of the fringe field in the VUV dipole is closely approximated by a linearly falling field 17.1 cm in length.

TABLE I. Average Multipole Terms in NSLS Dipoles Booster (Normalized to 1308 Amps)

Mag. #	$\frac{1}{L}\int Bd\ell$	$\frac{1}{L}\int B'd\ell$	$\frac{1}{L}\int B''d\ell$
1	12228.0 G	-12.5520 G/mm	-.070977 G/mm^2
2	12224.8	-12.4274	-.069746
3	12214.7	-12.5960	-.070102
4	12221.1	-12.6133	-.069448
5	12235.0	-12.5062	-.072070
6	12222.4	-12.4997	-.070367
7	12231.9	-12.5494	-.075140
8	12234.1	-12.4327	-.070289
	X-ray (Normalized to 1379 Amps)		
1	12173.7	.4288	-.009854
2	12152.7	.4241	-.010318
3	12157.2	.4180	-.010016
4	12155.9	.4327	-.009996
5	12150.7	.4210	-.009926
6	12148.2	.3936	-.009668
7	12155.6	.4041	-.009709
8	12161.0	.4168	-.009637
9	12175.8	.4344	-.010508
10	12184.6	.4701	-.010189
11	12163.5	.5024	-.011011
12	12170.8	.4586	-.011054
13	12175.1	.4383	-.010162
14	12177.9	.4767	-.010082
15	12178.4	.3619	-.009247
16	12185.8	.3512	-.010313
	VUV (Normalized to 1389 Amps)		
Mag. #	$\frac{1}{L}\int Bdx$	$\frac{1}{L}\int B'dx$	$\frac{1}{L}\int B''dx$
1	11888.2	.7268	-.008670
2	11899.7	.7134	-.009580
3	11899.4	.7386	-.008336
4	11897.8	.7078	-.012460
5	11907.3	.6903	-.010834
7	11902.0	.6032	-.006802
8	11903.0	.6551	-.013711

References

1. J. Galayda, R. N. Heese, H.C.H. Hsieh, H. Kapfer, "The NSLS Magnet System", IEEE Transactions on Nuclear Science, V. NS-26 No. 3, pp. 3919-3921 (1979).
2. R. Holsinger, "POISSON Group Programs Users Guide" Los Alamos, LAUR-76-2028 (10/21/78).
3. J. Galayda, "Curvature of the NSLS Dipole Magnets", NSLS Technical Note 29, (10/9/79).
4. G. Parzen, "Magnetic Fields for Transporting Charged Beams", BNL-50536, (January 1976).

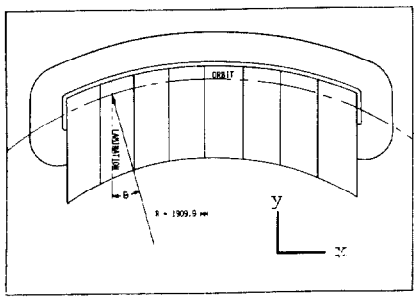

Fig. 1. NSLS VUV or booster dipole

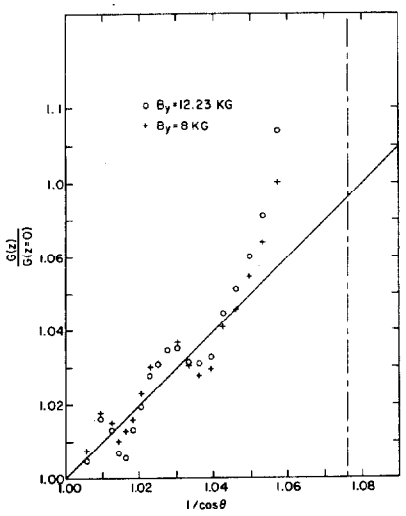

Fig. 2. NSLS booster dipole-variation of gradient

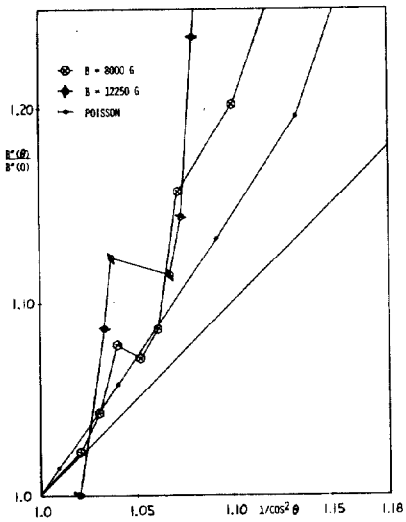

Fig. 3. NSLS booster dipole-variation of sextupole

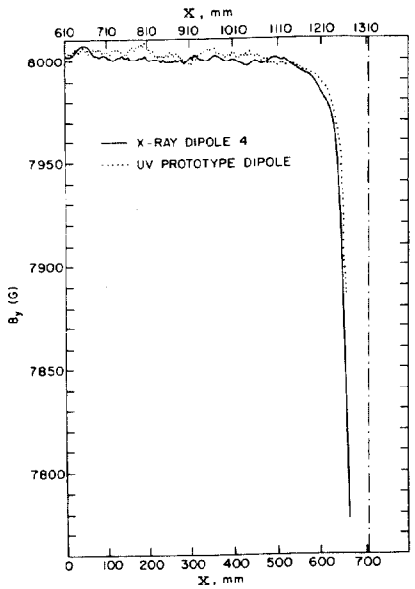

Fig. 4. NSLS VUV and X-ray dipoles central field vs. x, 8 KG

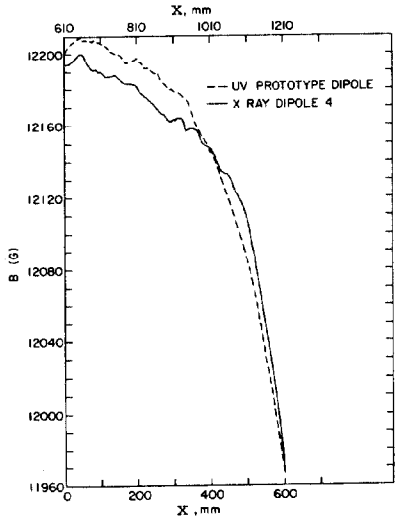

Fig. 5. NSLS VUV and X-ray dipoles central field vs. x, 12 KG

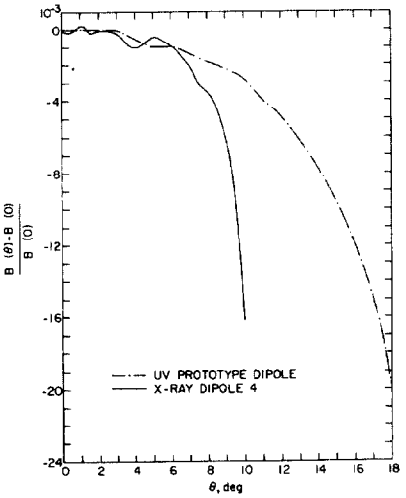

Fig. 6. NSLS VUV and X-ray dipoles central field vs. θ, 12 KG

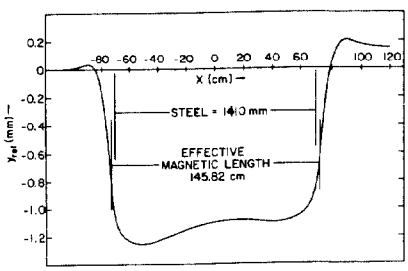

Fig. 7. NSLS VUV dipole tracking results - deviation from ideal orbit

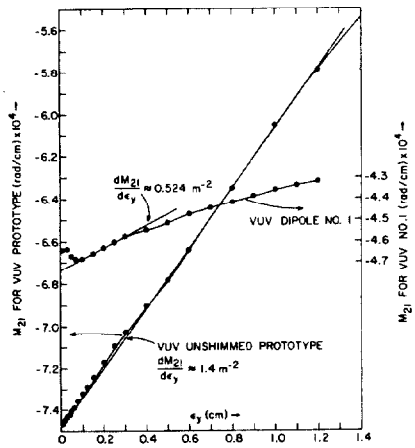

Fig. 8. NSLS VUV dipole tracking horizontal inverse focal length